

A Computational Simulation of Using Tungsten Gratings in Near-Field Thermophotovoltaic Devices

J. I. Watjen, X. L. Liu, B. Zhao, and Z. M. Zhang^{*}

George W. Woodruff School of Mechanical Engineering

Georgia Institute of Technology, Atlanta, GA 30332

Near-field thermophotovoltaic (NFTPV) devices have received much attention lately as an alternative energy harvesting system, whereby a heated emitter exchanges super-Planckian thermal radiation with a photovoltaic (PV) cell to generate electricity. This work describes the use of a grating structure to enhance the power throughput of NFTPV devices, while increasing the energy conversion efficiency by ensuring that a large portion of the radiation entering the PV cell is above the band gap. The device contains a high-temperature tungsten grating that radiates photons to a room-temperature $\text{In}_{0.18}\text{Ga}_{0.82}\text{Sb}$ PV cell through a vacuum gap of several tens of nanometers. Scattering theory is used along with the rigorous coupled-wave analysis to calculate the radiation energy exchange between the grating emitter and the TPV cell. A parametric study is performed by varying the grating depth, period, and ridge width in the range that can be fabricated using available fabrication technologies. It is found that the power output can be increased by 40% while improving the efficiency from 29.9% to 32.0% with a selected grating emitter as compared to the case of a flat tungsten emitter. Reasons for the enhancement are found to be due to the enhanced energy transmission coefficient close to the band gap. This work shows a possible way of improving NFTPV and sheds light on how grating structures interact with thermal radiation at the nanoscale.

Keywords: fluctuation-dissipation theory, gratings, near-field thermal radiation, thermophotovoltaic

Corresponding author: zhuomin.zhang@me.gatech.edu

1 Introduction

Near-field radiation heat transfer has been an exciting research avenue especially during the past decade [1-5]. As has been both theoretically and experimentally demonstrated, as two media with different temperatures are brought very close together, photon tunneling can greatly enhance the radiative energy transfer [6-12]. One promising application of near-field radiation is in thermophotovoltaic (TPV) energy conversion devices [13-18]. With this technology, a high-temperature source radiates electromagnetic thermal energy toward a photovoltaic (PV) cell and electrical current can be generated by photons whose energy is above the band gap of the PV material. Being a portable solid-state energy generation technique with no moving parts, TPVs can be used to recover waste heat from other energy generation technologies very conveniently, such as fuel cells or combustion chambers [19,20].

Compared to solar PV cells, TPV devices have an advantage whereby the heated source can be a micro/nanostructured material, and the emissivity can be tuned to align with the bandgap of the receiver. Thus, only above-band-gap radiation leaves the source and the overall energy conversion efficiency can be very high [21]. Periodic nanostructures have been proposed to shape the thermal emission for different applications with great success including one-dimensional gratings [22-24] as well as two-dimensional gratings and nanowires [25,26]. Work has been done to make the radiation energy of TPV emitter fall above the cell band gap by using thin films [27,28] or various nanostructures [20,29-33]. While these devices may be able to tune the radiation such that the efficiency exceeds solar PV devices, the power throughput per unit area is limited by the well-known Stefan-Boltzmann law.

Near-field thermophotovoltaics (NFTPVs) have been considered to eliminate this barrier by achieving orders of magnitude higher heat flux as the distance between the emitter and the PV

cell decreases well below the characteristic thermal wavelength [16]. Due to photon tunneling, radiation with very large transverse wavevectors can travel across the vacuum gap, resulting in tremendous amounts of energy transported into the PV cell for the generation of electron-hole pairs [34]. Recently, much attention has been going to optimize the radiative exchange in NFTPV devices by using a backside mirror [35], thin films [36], graphene [37,38], and nanowires [39]. Thus far, the analysis of NFTPV devices using structured emitters, especially employing numerically exact approaches, is lacking. Furthermore, the role of gratings in the near-field regime may behave differently than in the far field [40-44], making it compelling to investigate how gratings interact with the near-field energy harvesting processes.

The present study seeks to improve both the energy harvesting rate and efficiency in a NFTPV by using a periodic tungsten grating on a tungsten substrate as the thermal emitter. By adjusting the grating parameters, the near-field radiative transfer via photon tunneling can be greatly enhanced, especially at photon energies greater than the band gap of the $\text{In}_{0.18}\text{Ga}_{0.82}\text{Sb}$ PV cell with a band gap of 0.56 eV, as compared with the baseline case where the emitter is a plain tungsten. The radiative energy exchange and the electrical power output are calculated based on scattering theory. A parametric sweep of the period, height, and width of the grating is conducted over a large range, while maintaining practical values. A phenomenological study of the trends with the geometry parameters reveals insights behind the performance enhancement. Through the use of advanced simulations and analysis, this work aims at further understanding the role of nanostructures in near-field radiation and seeking a new avenue for TPV development.

2 Numerical Modeling

The NFTPV system employing a tungsten grating is schematically in Fig. 1. Here, the tungsten emitter is comprised of a one-dimensional tungsten grating and a semi-infinite tungsten substrate. The tungsten emitter is separated from a semi-infinite $\text{In}_{0.18}\text{Ga}_{0.82}\text{Sb}$ receiver by a nanoscale vacuum gap of a thickness d . The emitter and receiver extend infinitely in the x - and y -directions, with the emitter being periodic in the x -direction. The periodicity is governed by the grating period P , grating height H , and the strip width w . The filling ratio f is equal to w/P , which represents the relative size of the grating strip.

The radiative energy exchange between the emitter and receiver will occur over a temperature difference. The emitter temperature is prescribed as $T_1 = 2000$ K, such that the peak wavelength for the thermal radiation exchange is around $1.45 \mu\text{m}$. The receiver temperature is assumed to be at $T_2 = 300$ K. The optical properties of tungsten are taken from Palik [45] at room temperature, while the optical properties of $\text{In}_{0.18}\text{Ga}_{0.82}\text{Sb}$ are obtained from [45,46]. The near-field radiative heat flux between the tungsten emitter and PV cell can be obtained through the framework of scattering theory [43,44,47].

$$q'' = \int_0^{\infty} q''_{\omega}(\omega) d\omega \quad (1a)$$

where

$$q''_{\omega}(\omega) = \frac{\Theta(\omega, T_1) - \Theta(\omega, T_2)}{8\pi^3} \int_{-\infty}^{\infty} \int_{-\pi/P}^{\pi/P} \xi(\omega, k_x, k_y) dk_x dk_y \quad (1b)$$

is the spectral heat flux that depends on the temperatures of the emitter and the PV cell. Here, the function $\Theta(\omega, T)$ represents the average energy of Planck's oscillator at a given angular frequency and temperature, and $\xi(\omega, k_x, k_y)$ is the energy transmission coefficient that includes

both p-polarization and s-polarization. It should be noted that the energy transmission coefficient depends on the geometry and material properties but not directly on the temperatures. In order to obtain the wavevector and frequency-dependent energy transmission coefficient, the rigorous coupled-wave analysis (RCWA) is used. The integration limits on k_x are restricted to the first Brillouin zone due to the periodicity in the x direction. The details of this method can be found in [48]. For a planar tungsten emitter, the transmission coefficient can be calculated according to Fresnel's coefficients and the integration for k_x is from $-\infty$ to $+\infty$.

The computation of the energy transmission coefficient is a lengthy process prone to discretization errors, and the parameters used are outlined here. RCWA is used to find the reflection coefficient matrixes of dimension $2(2N+1)$ for both the emitter and receiver. Here N is the maximum diffraction order considered in the calculation, and 35 orders were used in this work. The angular frequency ω is logarithmically spaced with 80 values over a range from 2.3×10^{14} to 4.5×10^{15} rad/s. The wavevectors k_x and k_y are evenly spaced with 43 values for k_x and 71 values for k_y . Using these parameters, the calculation time for a specified geometry on a dual eight-core Xeon E5-2687W workstation is over two hours. When doubling the numbers values for frequency, k_x , and k_y , the change of radiative energy flux is about 1 to 2 percent, and change of energy conversion efficiency is within 0.2%. This fine mesh is used only for several selected cases (shown in Table 1), and the numerical uncertainty is believed to be within 1%.

Since the geometries of the emitter substrate and PV cell receiver are semi-infinite, it is assumed that each absorbed photon by the receiver can excite an electron-hole pair as long as the photon energy exceeds the $\text{In}_{0.18}\text{Ga}_{0.82}\text{Sb}$ cell band gap of 0.56 eV. Furthermore, surface recombination and bulk recombination are neglected, *i.e.*, 100% quantum efficiency is assumed.

While this is expected to over-predict the actual near-field TPV performance [14], the intent of this work is to optimize the tungsten grating emitter, and PV cell performance serves mainly as a metric for comparison of the relative performance. The maximum electrical power output per unit area is evaluated by

$$P_{\text{el}} = J_{\text{sc}} V_{\text{oc}} FF \quad (2)$$

where J_{sc} is the short circuit current density, V_{oc} is the open circuit voltage, and FF is the fill factor [49]. Since 100% quantum efficiency is assumed, J_{sc} can be found from

$$J_{\text{sc}} = \int_{\omega_g}^{\infty} \frac{e}{\hbar \omega} q''(\omega) d\omega \quad (3)$$

Below the frequency ω_g that corresponds to the band gap, no photon current can be generated.

The open circuit voltage V_{oc} and fill factor FF , which are functions of the carrier concentrations, diffusivities, and lifetimes, can be obtained using formulations described in Ref. [14]. Finally, the energy conversion efficiency is the ratio of electrical power output to amount of the radiative energy exchanged, *i.e.*, $\eta = P_{\text{el}}/q''$. Here, the net heat flux q'' is the amount of thermal energy leaving the high-temperature source at temperature T_1 , and subsequently, η is the thermal efficiency of the NFTPV system.

3 Results and Discussion

To identify the best grating performances, a parametric sweep is performed for P , H , and f with a fixed $d = 20$ nm. This gap spacing d is chosen to illustrate the behavior in the very near-field. The grating parameters are allowed to vary in a wide range: P between 10 nm and 2000 nm, H between 10 nm to 1000 nm, and f between 0.1 and 0.9, representing approximately 400

different grating geometries. Figure 2 shows the maximum power output and efficiency over a large range of grating period and height. Here, for each point of P and H shown, the filling ratio f is optimized individually to get the highest power output or conversion efficiency. Figure 2(a) demonstrates that the high power output has a very clear trend towards grating geometries with smaller P and greater H . Although it would appear that the parametric study should continue in this direction, these geometries represent a class of gratings that are extremely difficult to fabricate, with sub-nanometer minimum feature sizes at aspect ratios verging on 1000. Here the aspect ratio is defined to be the ratio of the grating height to the minimum feature size. Figure 2(b) illustrates a more complicated topology when only looking at the efficiencies. It is important to note that the values of the filling ratio at the same period and grating height are different in Figs. 2(a) and 2(b), so comparison is difficult between the two plots. However, it can be seen that there are certain regimes where the performance is promising without extremely hard-to-make geometric dimensions. In some regimes, the location with higher efficiency does coincide with that of high output power. The maximum possible power typically increases with the grating height, though there may be a lack in efficiency.

For each permutation of parameters, the power output P_{el} and conversion efficiency η for the NFTPV system are compared to the baseline case of a plain tungsten emitter. The results for a planar tungsten substrate are already fairly superior with a power output P_{el} of 768 kW/m^2 and efficiency η of 29.9% at 20 nm gap spacing, and a majority of the grating geometries are not able to outperform the baseline case in both power and efficiency. Many of the structures analyzed are able to exceed the electrical power output, but at the cost of a reduced efficiency. Furthermore, a majority of the grating structures that have an efficiency exceeding the plain tungsten case require feature sizes of a few nanometers. When selecting geometry parameters

with good performance, the minimum feature size is kept as 10 nm, which is possible to fabricate using existing technologies, *e.g.*, electron beam lithography, and a maximum aspect ratio of 35, a value achievable by either deep reactive ion etching (RIE) or inductively coupled plasma RIE. This limits the maximum power output and efficiency greatly. Nevertheless, there still exist a large number of combined geometries that yield good performance. Qualitative analysis of the spectral energy distribution absorbed by the receiver is also used to identify promising grating parameters.

A selection of grating geometries with fairly good performance for both the power output and energy efficiency is listed in Table 1. The four cases correspond to grating period from 50 to 200 nm. All the selected cases have power output and efficiencies higher than that with a plain tungsten emitter. The best performance that gives both the highest power output and conversion efficiency is for case 1 with $P = 50$ nm, $H = 500$ nm, and $f = 0.8$. This case will be investigated in detail in the rest of this work, including gap spacing effect and further parameter tuning by varying individual parameters while fixing the rest. It should be noted that geometries with lower periods and higher filling ratios may outperform this combination by up to 20%; however, they are too difficult to fabricate using presently available techniques.

The NFTPV performance with the grating of the selected geometries according to case 1 of Table 1 is shown in Fig. 3 over a large range of gap distances. The power output and efficiency for planar tungsten substrate are also shown for comparison. It is seen that the grating has a higher power output over all gap distances. At $d = 100$ nm, P_{el} of the grating emitter is nearly twice that of the planar emitter (375 kW/m² for grating versus 188 kW/m² for plain tungsten). At extreme nanometer distance, the near-field interaction tends to become localized [43,50]. As a result, the near-field energy exchange with grating is approximately equal to that

for planar substrate multiplied by the filling ratio. Thus, the difference in the power output becomes smaller at $d = 10$ nm. Further reducing the gap spacing to a few nanometers can result in a reverse of the power output when grating yields a smaller power output.

In terms of the energy conversion efficiency, the grating emitter outperforms planar emitter when the gap spacing is below about 140 nm, and the improvement increases with decreasing gap spacing down to 20 nm or so. At $d = 20$ nm, the grating has a modest improvement in both power and efficiency, providing $P_{\text{el}} = 1078 \text{ kW/m}^2$ (which is 40% greater than that of a planar emitter) and $\eta = 32.0\%$ (which is 2.1% greater than that for a planar emitter). At $d = 50$ nm, the power output increases by 68% while the efficiency increases by 1.6%. While the power output is almost doubled at $d = 100$ nm with the grating emitter, the efficiency only increases by 1.0%.

Due to wave interference effects, the power output has a maximum and minimum at gap distances of 500 nm and 800 nm, respectively, for both the grating structure and plain tungsten. The latter has been observed previously, *e.g.*, Ref. [14]. As the spacing beyond 140 nm, the grating structure underperforms the flat tungsten in conversion efficiency. This suggests that grating enhances photon tunneling at energies lower than the band gap more than it does for photons at energies higher than the band gap. Subsequently, while the power output increases, the conversion efficiency decreases until the gap spacing exceeds about 1.6 μm and gradually reaches the far-field limit. For gap spacing beyond approximately 2 μm , the tungsten grating behaves as a selective far-field emitter that can enhance both the power output and conversion efficiency. Note that the far-field power output, say at $d = 10 \mu\text{m}$, is only 57.1 kW/m^2 with grating and 33.4 kW/m^2 without grating. For the remainder of this work, all calculations will be based on $d = 20$ nm, where the grating structure has prominent performance advantages over

plain tungsten, and furthermore, near-field effects can significantly increase the power output as well as the conversion efficiency.

It is important to investigate how each parameter influences the NFTPV system performance to get a good understanding of the geometric effects. To this end, the dependence of P_{el} and η on each geometric parameter is plotted in Fig. 4. Here, the default geometries correspond to case 1 of Table 1 and only one parameter is allowed to vary over a large range. The effect of filling ratio is shown in Fig. 4(a). As the filling ratio increases, both the power and efficiency rises. The efficiency reaches a maximum at about $f = 0.8$, where the power continues to increase somewhat as f further increases up to 0.9. Note that $f = 1$ represents the planar geometry without grating since the tungsten grating is on a semi-infinite tungsten substrate. Because the grating period is fixed, a larger filling ratio means a narrower grating slit; hence, the narrowness of the grating slit plays a key role in the enhanced performance. As shown in Fig. 4(b), when the grating period is less than 500 nm, the efficiency increases with decreasing P , especially at very small periods. However, when the period is less than 50 nm, the slit width for $f = 0.8$ is smaller than 10 nm that is challenging to fabricate. Interestingly, the electric power reaches a maximum of 1.08 MW/m^2 at $P = 100 \text{ nm}$ with an efficiency of 30.6%, which is slightly higher than the case without grating. The power decreases toward larger periods. When the period is large enough, approaching the characteristic wavelength of thermal radiation at 2000 K, the effects of the grating vanish, and the heat flux tends towards an average of the radiation from the top and bottom of the grating [41]. The efficiency is generally less than 29% for grating period larger than 300 nm, though it slightly increases beyond $P = 500 \text{ nm}$. In the range $50 \text{ nm} < P < 100 \text{ nm}$, the grating structure can achieve significant enhanced power and somewhat increased efficiency over the planar counterpart. In Fig. 4(c), a maximum in the efficiency can be

seen at a grating height close to 500 nm while the power continues to increase with deeper gratings, suggesting that deep-grating cavity resonance modes may play a part in the enhancement. This also supports the trend of increased performance at large filling ratios, as the slit width becomes very narrow. In the case of a deep grating with a narrow slit, cavity resonance modes can be excited [24], and may increase the energy throughput. For optimal performance, the grating height should be between 400 nm and 600 nm. The results showing in Fig. 4 clearly suggest that there is a relatively large fabrication tolerance because high performance can be maintained as long as the the default parameters are not deviated significantly.

To better understand the mechanisms for the enhancement of using a grating over the planar tungsten case, the spectral response is analyzed. The energy transmission coefficient $\xi(\omega, k_x, k_y)$ for the plain tungsten and the grating structure is shown in Figs. 5(a) and 5(b), respectively, by fixing $k_y = 0$. The wavevector k_x is normalized by π/P for convenience in both plots, and the light line $k_x = k_0$ is also shown. Although k_x for planar tungsten is not limited to π/P , the maximum k_x for plain tungsten is chosen to be π/P for easy comparison with the grating case. As shown in Fig. 5(a), this value is sufficiently high since ξ is already very small near this limit. It should be noted that cylindrical coordinates are used for plain tungsten to integrate over the tangential wavevector space for calculations of the radiative heat flux and power output [1]. The integration limit is extended until convergence is reached. Notice that once the dielectric functions and geometric parameters are specified, the contour plots are invariant to temperatures. The band gap of $\text{In}_{0.18}\text{Ga}_{0.82}\text{Sb}$ is 0.56 eV ($\omega_g = 8.4 \times 10^{14}$ rad/s), and only photons with energies greater than the band gap are able to generate electron-hole pairs. As shown in Fig. 5(a), the planar tungsten system can already support a high energy transmission

coefficient above the band gap. Therefore, it is challenging to outperform the planar tungsten substrate dramatically.

Excitation of surface plasmon polaritons (SPPs) at the vacuum-metal interface usually has a dominant contribution to the near-field radiative energy exchange [13,51]. However, tungsten, unlike many other metals, has a high dc resistivity and scattering rate and intraband transitions in the visible and near infrared [52]. The resulting dielectric function has a very high loss, *i.e.*, the imaginary part of the dielectric function is about 20 at $\omega > 1.7 \times 10^{15}$ rad/s and even larger at lower frequencies. As shown in Fig. 5(a), there is a region featured with high energy transmission coefficients just lying on the right side of the light line. This regime extends from 1.1×10^{15} rad/s all the way toward the frequency upper bound. Note that the real part of the dielectric function of tungsten $\text{Re}(\epsilon)$ becomes positive at frequencies higher than approximately 2.0×10^{15} rad/s. Subsequently, the excitation condition of SPPs, which requires the permittivities to have different signs at the interface, cannot be satisfied. Even at $\omega = 1.96 \times 10^{15}$ rad/s where $\text{Re}(\epsilon) = -1$ for tungsten, which is the condition for excitation of SPPs at the vacuum-tungsten interface, no obvious resonance-assisted high energy transmission coefficients show up. Previous studies by Basu and Zhang [53] and Liu et al. [54] also noticed that the peak of the energy transmission coefficient may not occur at the frequency where $\text{Re}(\epsilon) = -1$ if the loss is sufficiently high. Liu et al. [55] showed that the cutoff wavevector, beyond which the contribution to photon tunneling becomes negligible, decreases with the increasing loss. The high loss of tungsten prevents the inside fluctuational current to couple with very high wavevectors and prohibits SPPs to be excited at the vacuum-tungsten interface. Nevertheless, there exist large transmission coefficients outside the light line where photon tunneling coefficient peaks, though not associated with any resonance phenomena. It should be noted that

the PV cell serves as a loss dielectric in this region and has less effects on the ξ . This has been verified by considering the energy transmission coefficients between two tungsten plates or between two PV cell plates. Though not shown here, the shape between two tungsten plates assembles that of Fig. 5(a) at $\omega > 1.9 \times 10^{15}$ rad/s. Therefore, the enhanced power output and radiative energy exchange at $d = 20$ nm over the far-field case cannot be attributed to the excitation of SPPs, but are mainly due to the photon tunneling of evanescent waves in a broad frequency region. Note that both s- and p-polarizations are included in Fig. 5(a). They have comparable contributions (55% for p-polarization and 45% for s-polarization) to the radiative energy exchange for the plain tungsten.

For the tungsten grating, it is hard to identify the contributions from individual polarization due to the polarization coupling effects and the numerical algorithm used. Figure 5(b) shows that the energy transmission coefficient for the grating structure. Compared with Fig. 5(a), it can be seen that ξ for the grating structure is higher in a broad frequency and wavevector ranges, especially in the frequency region from 1.2×10^{15} to 2.5×10^{15} rad/s. Both the radiative heat flux and the electric power output are enhanced with gratings, and the enhancement of the power output is slightly higher, resulting in the somewhat increased conversion efficiency. While for plain tungsten, Fig. 5(a) is sufficient to describe the energy transmission coefficient versus the transverse wavevector due to isotropy, Fig. 5(b) is only for $k_y = 0$ and it is necessary to investigate the effect of k_y on the transmission coefficient as well.

To explore the energy transmission coefficients at nonzero k_y values, $\xi(\omega, k_x, k_y)$ is the integrated over k_x , such that

$$\xi_{\omega, k_y} = \frac{1}{k_0} \int_{-\pi/P}^{\pi/P} \xi(\omega, k_x, k_y) dk_x \quad (5)$$

where k_0 is the wavevector in vacuum. Note that the integration limits for plain grating are from $-\infty$ to ∞ . The calculated ξ_{ω, k_y} are shown in Fig. 6 for both plain tungsten and tungsten grating as functions of ω and k_y / k_0 . When $k_y = 0$, the values along the vertical axis in Figs. 6(a) and 6(b) correspond to the integration over a horizontal line of the color contour of Figs. 5(a) and 5(b), respectively. The enhancement of grating becomes clear especially towards large k_y and lower frequencies. Subsequently, both the heat flux and the electric power output are enhanced.

To better understand the mechanism accounting for the enhanced conversion efficiency with gratings, it is helpful to define a spectral energy transmission coefficient, which is obtained by integrating the energy transmission coefficient over all wavevectors:

$$\xi_{\omega} = \frac{1}{2\pi k_0^2} \int_{-\infty}^{\infty} \int_{-\pi/P}^{\pi/P} \xi(\omega, k_x, k_y) dk_x dk_y \quad (6)$$

The Stefan-Boltzmann law will be recovered if $\xi_{\omega}=1$ is substituted into Eq. (1). Thus, the physical significance of ξ_{ω} is that when $\xi_{\omega} > 1$, the combined contribution of propagating waves and evanescent waves exceeds the blackbody radiation at the specified frequency. Note that the integration limits of $\pm\pi/P$ are substituted by $\pm\infty$ when applying Eq. (6) for the planar case. As shown in Fig. 7, the tungsten grating gives rise to a peak ξ_{ω} at 1.2×10^{15} rad/s, which corresponds to the low-frequency bump in Fig. 6(b). This feature is stronger with larger grating heights or narrower grating slits, so it is plausible that cavity resonance is responsible for the enhancement [24]. Comparing the cases with and without tungsten grating, it is clear that the spectral energy transmission coefficient is higher especially below 2.0×10^{15} rad/s, in consistent

with Fig. 6. Note that the angular frequency corresponding to the bandgap energy is 8.4×10^{14} rad/s, as shown with the vertical dotted line in Fig. 7. Hence, the advantage that the grating structure has over the plain tungsten is that the spectral energy transmission coefficient is not only higher, but also has been pushed closer to the PV band gap. Because the excess energy of the higher frequency photons beyond the band gap is lost due to thermalization processes, the grating system yields a higher energy conversion efficiency due to less thermalization loss.

4 Conclusions

Using the exact scattering matrix approach, we have simulated the near-field radiative energy exchange between tungsten gratings and an $\text{In}_{0.18}\text{Ga}_{0.82}\text{Sb}$ PV cell. The power output and energy conversion efficiency of the NFTPV system have been calculated by assuming 100% quantum efficiency and compared with the flat tungsten case. Through a parametric sweep of grating geometries, several suitable emitters have been identified that can outperform the baseline case. When $P = 50$ nm, $H = 500$ nm, and $f = 0.8$, the electrical output power was 1078 kW/m^2 with an efficiency of 32.0% at $d = 20$ nm, showing an improvement over the planar case by 40% and 2.1% for power output and conversion efficiency, respectively. The enhanced energy transmission coefficient especially near the bandgap frequency is found to be the reason accounting for the performance enhancement. This work helps identify efficient nanostructured NFTPV devices as well as gain insights into near-field radiation with nano-grating structures.

Acknowledgments

This work was supported by the U.S. Department of Energy, Office of Science, Basic Energy Sciences (DE-FG02-06ER46343).

Nomenclature

d	vacuum gap spacing, m
e	charge of an electron, 1.602×10^{-19} C
f	filling ratio, w/P
FF	fill factor
\hbar	reduced Planck's constant, 1.055×10^{-34} J·s
H	grating height, m
J_{sc}	short circuit current, $A \cdot m^{-2}$
k	wavevector, m^{-1}
k_0	wavevector in vacuum, m^{-1}
N	number of diffraction orders
P	grating period, m
P_{el}	electrical power output per unit area, $W \cdot m^{-2}$
q''	heat flux, $W \cdot m^{-2}$
q''_{ω}	spectral heat flux, $W \cdot m^{-2} \cdot rad^{-1} \cdot s$
T	temperature, K
V_{oc}	open circuit voltage, V
w	grating strip width, m

Greek Symbols

ε	dielectric function
η	energy conversion efficiency

Θ	mean energy of the Planck oscillator, J
ξ	energy transmission coefficient
ω	angular frequency, $\text{rad}\cdot\text{s}^{-1}$
ω_g	angular frequency corresponding to the band gap, $\text{rad}\cdot\text{s}^{-1}$

References

- [1] Zhang, Z. M., 2007, *Nano/Microscale Heat Transfer*, McGraw-Hill, New York.
- [2] Xuan, Y., 2014, "An Overview of Micro/Nanoscaled Thermal Radiation and Its Applications," *Phot. Nano. Fund. Appl.*, **12**, pp. 93-113.
- [3] Liu, X. L., Wang, L. P., and Zhang, Z. M., 2015, "Near-Field Thermal Radiation: Recent Progress and Outlook," *Nanoscale Microscale Thermophys. Eng.*, **19**, pp. 98-126.
- [4] Cahill, D. G., Braun, P. V., Chen, G., Clarke, D. R., Fan, S., Goodson, K. E., Keblinski, P., King, W. P., Mahan, G. D., Majumdar, A., Maris, H. J., Phillpot, S. R., Pop, E., and Shi, L., 2014, "Nanoscale Thermal Transport: II. 2003–2012," *Appl. Phys. Rev.*, **1**, p. 011305.
- [5] Biehs, S.-A., Ben-Abdallah, P., and Rosa, F. S., 2012, "Nanoscale Radiative Heat Transfer and Its Applications," in *Infrared Radiation*, V. Morozhenko (ed.), InTech, Rijeka, Croatia, Chap. 1.
- [6] Rytov, S. M., Kravtsov, Y. A., and Tatarskii, V. I., 1989, *Principles of Statistical Radiophysics*, Springer, New York.
- [7] Kittel, A., Muller-Hirsch, W., Parisi, J., Biehs, S.-A., Reddig, D., and Holthaus, M., 2005, "Near-Field Heat Transfer in a Scanning Thermal Microscope," *Phys. Rev. Lett.*, **95**, p. 224301.
- [8] Rousseau, E., Siria, A., Jourdan, G., Volz, S., Comin, F., Chevrier, J., and Greffet, J.-J., 2009, "Radiative Heat Transfer at the Nanoscale," *Nat. Photonics*, **3**, pp. 514-517.
- [9] Shen, S., Narayanaswamy, A., and Chen, G., 2009, "Surface Phonon Polaritons Mediated Energy Transfer between Nanoscale Gaps," *Nano Lett.*, **9**, pp. 2909-2913.
- [10] Song, B., Ganjeh, Y., Sadat, S., Thompson, D., Fiorino, A., Fernández-Hurtado, V., Feist, J., Garcia-Vidal, F. J., Cuevas, J. C., Reddy, P., and Meyhofer, E., 2015, "Enhancement of Near-Field Radiative Heat Transfer Using Polar Dielectric Thin Films," *Nat. Nanotechnol.*, **10**, pp. 253-258.

- [11] St-Gelais, R., Guha, B., Zhu, L., Fan, S., and Lipson, M., 2014, "Demonstration of Strong Near-Field Radiative Heat Transfer between Integrated Nanostructures," *Nano Lett.*, **14**, pp. 6971-6975.
- [12] Lim, M., Lee, S. S., and Lee, B. J., 2015, "Near-Field Thermal Radiation between Doped Silicon Plates at Nanoscale Gaps," *Phys. Rev. B*, **91**, p. 195136.
- [13] Basu, S., Chen, Y.-B., and Zhang, Z. M., 2007, "Microscale Radiation in Thermophotovoltaic Devices: A Review," *Int. J. Energy Res.*, **31**, pp. 689-716.
- [14] Park, K., Basu, S., King, W. P., and Zhang, Z. M., 2008, "Performance Analysis of Near-Field Thermophotovoltaic Devices Considering Absorption Distribution," *J. Quant. Spectrosc. Radiat. Transfer*, **109**, pp. 305-316.
- [15] Francoeur, M., Vaillon, R., and Mengüç, M. P., 2011, "Thermal Impacts on the Performance of Nanoscale-Gap Thermophotovoltaic Power Generators," *IEEE Trans. Energy Convers.*, **26**, pp. 686-698.
- [16] Laroche, M., Carminati, R., and Greffet, J.-J., 2006, "Near-Field Thermophotovoltaic Energy Conversion," *J. Appl. Phys.*, **100**, p. 063704.
- [17] Narayanaswamy, A., and Chen, G., 2003, "Surface Modes for Near Field Thermophotovoltaics," *Appl. Phys. Lett.*, **82**, pp. 3544-3546.
- [18] Dimatteo, R. S., Greiff, P., Finberg, S. L., Young-Waithe, K. A., Choy, H. K. H., Masaki, M. M., and Fonstad, C. G., 2001, "Enhanced Photogeneration of Carriers in a Semiconductor Via Coupling across a Nonisothermal Nanoscale Vacuum Gap," *Appl. Phys. Lett.*, **79**, pp. 1894-1896.
- [19] Yang, W., Chou, S., Shu, C., Xue, H., Li, Z., Li, D., and Pan, J., 2003, "Microscale Combustion Research for Application to Micro Thermophotovoltaic Systems," *Energy Convers. Manage.*, **44**, pp. 2625-2634.
- [20] Bermel, P., Ghebrebrhan, M., Chan, W., Yeng, Y. X., Araghchini, M., Hamam, R., Marton, C. H., Jensen, K. F., Soljačić, M., and Joannopoulos, J. D., 2010, "Design and Global Optimization of High-Efficiency Thermophotovoltaic Systems," *Opt. Express*, **18**, pp. A314-A334.

- [21] Datas, A., 2015, "Optimum Semiconductor Bandgaps in Single Junction and Multijunction Thermophotovoltaic Converters," *Sol. Energy Mater. Sol. Cells*, **134**, pp. 275-290.
- [22] Greffet, J.-J., Carminati, R., Joulain, K., Mulet, J.-P., Mainguy, S., and Chen, Y., 2002, "Coherent Emission of Light by Thermal Sources," *Nature*, **416**, pp. 61-64.
- [23] Wang, H., Yang, Y., and Wang, L. P., 2014, "Switchable Wavelength-Selective and Diffuse Metamaterial Absorber/Emitter with a Phase Transition Spacer Layer," *Appl. Phys. Lett.*, **105**, p. 071907.
- [24] Zhao, B. and Zhang, Z. M., 2014, "Study of Magnetic Polaritons in Deep Gratings for Thermal Emission Control," *J. Quant. Spectrosc. Radiat. Transfer*, **135**, pp. 81-89.
- [25] Liu, X. L., Wang, L. P., and Zhang, Z. M., 2013, "Wideband Tunable Omnidirectional Infrared Absorbers Based on Doped-Silicon Nanowire Arrays," *ASME J. Heat Transfer*, **135**, p. 061602.
- [26] Lee, B. J., Chen, Y.-B., Han, S., Chiu, F.-C., and Lee, H. J., 2014, "Wavelength-Selective Solar Thermal Absorber with Two-Dimensional Nickel Gratings," *ASME J. Heat Transfer*, **136**, p. 072702.
- [27] Rephaeli, E., and Fan, S., 2009, "Absorber and Emitter for Solar Thermo-Photovoltaic Systems to Achieve Efficiency Exceeding the Shockley-Queisser Limit," *Opt. Express*, **17**, pp. 15145-15159.
- [28] Lenert, A., Bierman, D. M., Nam, Y., Chan, W. R., Celanović, I., Soljačić, M., and Wang, E. N., 2014, "A Nanophotonic Solar Thermophotovoltaic Device," *Nat. Nanotechnol.*, **9**, pp. 126-130.
- [29] Wu, C., Neuner Iii, B., John, J., Milder, A., Zollars, B., Savoy, S., and Shvets, G., 2012, "Metamaterial-Based Integrated Plasmonic Absorber/Emitter for Solar Thermo-Photovoltaic Systems," *J. Opt.*, **14**, p. 024005.
- [30] Wang, L. P., and Zhang, Z. M., 2012, "Wavelength-Selective and Diffuse Emitter Enhanced by Magnetic Polaritons for Thermophotovoltaics," *Appl. Phys. Lett.*, **100**, p. 063902.

- [31] Yeng, Y. X., Chan, W. R., Rinnerbauer, V., Joannopoulos, J. D., Soljačić, M., and Celanovic, I., 2013, "Performance Analysis of Experimentally Viable Photonic Crystal Enhanced Thermophotovoltaic Systems," *Opt. Express*, **21**, pp. A1035-A1051.
- [32] Kohiyama, A., Shimizu, M., Kobayashi, H., Iguchi, F., and Yugami, H., 2014, "Spectrally Controlled Thermal Radiation Based on Surface Microstructures for High-Efficiency Solar Thermophotovoltaic System," *Energy Procedia*, **57**, pp. 517-523.
- [33] Zhao, B., Wang, L. P., Shuai, Y., and Zhang, Z. M., 2013, "Thermophotovoltaic Emitters Based on a Two-Dimensional Grating/Thin-Film Nanostructure," *Int. J. Heat Mass Transfer*, **67**, pp. 637-645.
- [34] Bernardi, M. P., Dupré, O., Blandre, E., Chapuis, P.-O., Vaillon, R., and Francoeur, M., 2015, "Impacts of Propagating, Frustrated and Surface Modes on Radiative, Electrical and Thermal Losses in Nanoscale-Gap Thermophotovoltaic Power Generators," *Sci. Report*, **5**, p. 011626.
- [35] Bright, T. J., Wang, L. P., and Zhang, Z. M., 2014, "Performance of Near-Field Thermophotovoltaic Cells Enhanced with a Backside Reflector," *ASME J. Heat Transfer*, **136**, p. 062701.
- [36] Tong, J. K., Hsu, W.-C., Huang, Y., Boriskina, S. V., and Chen, G., 2015, "Thin-Film 'Thermal Well' Emitters and Absorbers for High-Efficiency Thermophotovoltaics," *Sci. Report*, **5**, p. 010661.
- [37] Messina, R. and Ben-Abdallah, P., 2013, "Graphene-Based Photovoltaic Cells for Near-Field Thermal Energy Conversion," *Sci. Report*, **3**, p. 001383.
- [38] Ilic, O., Jablan, M., Joannopoulos, J. D., Celanovic, I., and Soljačić, M., 2012, "Overcoming the Black Body Limit in Plasmonic and Graphene Near-Field Thermophotovoltaic Systems," *Opt. Express*, **20**, pp. A366-A384.
- [39] Chang, J.-Y., Yang, Y., and Wang, L. P., 2015, "Tungsten Nanowire Based Hyperbolic Metamaterial Emitters for Near-Field Thermophotovoltaic Applications," *Int. J. Heat Mass Transfer*, **87**, pp. 237-247.

- [40] Rodriguez, A. W., Ilic, O., Bermel, P., Celanovic, I., Joannopoulos, J. D., Soljačić, M., and Johnson, S. G., 2011, "Frequency-Selective Near-Field Radiative Heat Transfer between Photonic Crystal Slabs: A Computational Approach for Arbitrary Geometries and Materials," *Phys. Rev. Lett.*, **107**, p. 114302.
- [41] Liu, X. L., and Zhang, Z. M., 2015, "Near-Field Thermal Radiation between Metasurfaces," *ACS Photon.*, **2**, p. 1320.
- [42] Guérout, R., Lussange, J., Rosa, F. S. S., Hugonin, J. P., Dalvit, D. A. R., Greffet, J.-J., Lambrecht, A., and Reynaud, S., 2012, "Enhanced Radiative Heat Transfer between Nanostructured Gold Plates," *Phys. Rev. B*, **85**, p. 180301.
- [43] Lussange, J., Guérout, R., Rosa, F. S. S., Greffet, J.-J., Lambrecht, A., and Reynaud, S., 2012, "Radiative Heat Transfer between Two Dielectric Nanogratings in the Scattering Approach," *Phys. Rev. B*, **86**, p. 085432.
- [44] Liu, X. L., and Zhang, Z. M., 2014, "Graphene-Assisted Near-Field Radiative Heat Transfer between Corrugated Polar Materials," *Appl. Phys. Lett.*, **104**, p. 251911.
- [45] Palik, E. D. (ed.), 1998, *Handbook of Optical Constants of Solids*, Vol. 1, Academic Press, San Diego.
- [46] González-Cuevas, J. A., Refaat, T. F., Abedin, M. N., and Elsayed-Ali, H. E., 2006, "Modeling of the Temperature-Dependent Spectral Response of $\text{In}_{1-x}\text{Ga}_x\text{Sb}$ Infrared Photodetectors," *Opt. Eng.*, **45**, p. 044001.
- [47] Liu, X. L., and Zhang, Z. M., 2015, "Giant Enhancement of Nanoscale Thermal Radiation Based on Hyperbolic Graphene Plasmons," *Appl. Phys. Lett.*, **107**, p. 143114.
- [48] Lambrecht, A., and Marachevsky, V. N., 2008, "Casimir Interaction of Dielectric Gratings," *Phys. Rev. Lett.*, **101**, p. 160403.
- [49] Ashcroft, N. W., and Mermin, N. D., 1976, *Solid State Physics*, Holt, Rinehart and Winston, New York.
- [50] Liu, X. L., Zhao, B., and Zhang, Z. M., 2015, "Enhanced Near-Field Thermal Radiation and Reduced Casimir Stiction between Doped-Si Gratings," *Phys. Rev. A*, **91**, p. 062510.

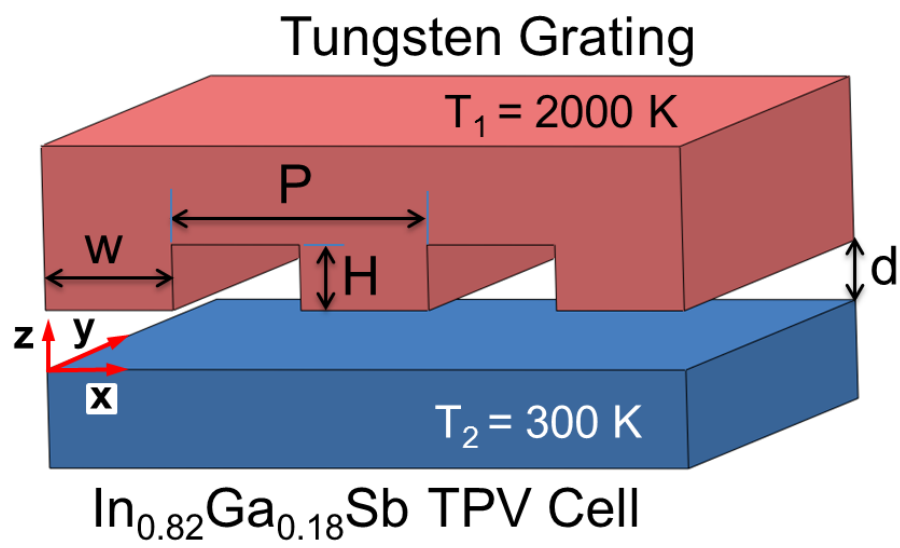
- [51] Joulain, K., Mulet, J.-P., Marquier, F., Carminati, R., and Greffet, J.-J., 2005, "Surface Electromagnetic Waves Thermally Excited: Radiative Heat Transfer, Coherence Properties and Casimir Forces Revisited in the Near Field," *Surf. Sci. Report*, **57**, pp. 59-112.
- [52] Watjen, J. I., Bright, T. J., Zhang, Z. M., Muratore, C., and Voevodin, A. A., 2013, "Spectral Radiative Properties of Tungsten Thin Films," *Int. J. Heat Mass Transfer*, **61**, pp. 106-113.
- [53] Basu, S., and Zhang, Z. M., 2009, "Maximum Energy Transfer in Near-Field Thermal Radiation at Nanometer Distances," *J. Appl. Phys.*, **105**, p. 093535.
- [54] Liu, B., Shi, J., Liew, K., and Shen, S., 2014, "Near-Field Radiative Heat Transfer for Si Based Metamaterials," *Opt. Commun.*, **314**, pp. 57-65.
- [55] Liu, X. L., Bright, T. J., and Zhang, Z. M., 2014, "Application Conditions of Effective Medium Theory in Near-Field Radiative Heat Transfer between Multilayered Metamaterials," *ASME J. Heat Transfer*, **136**, p. 092703.

Figure Captions:

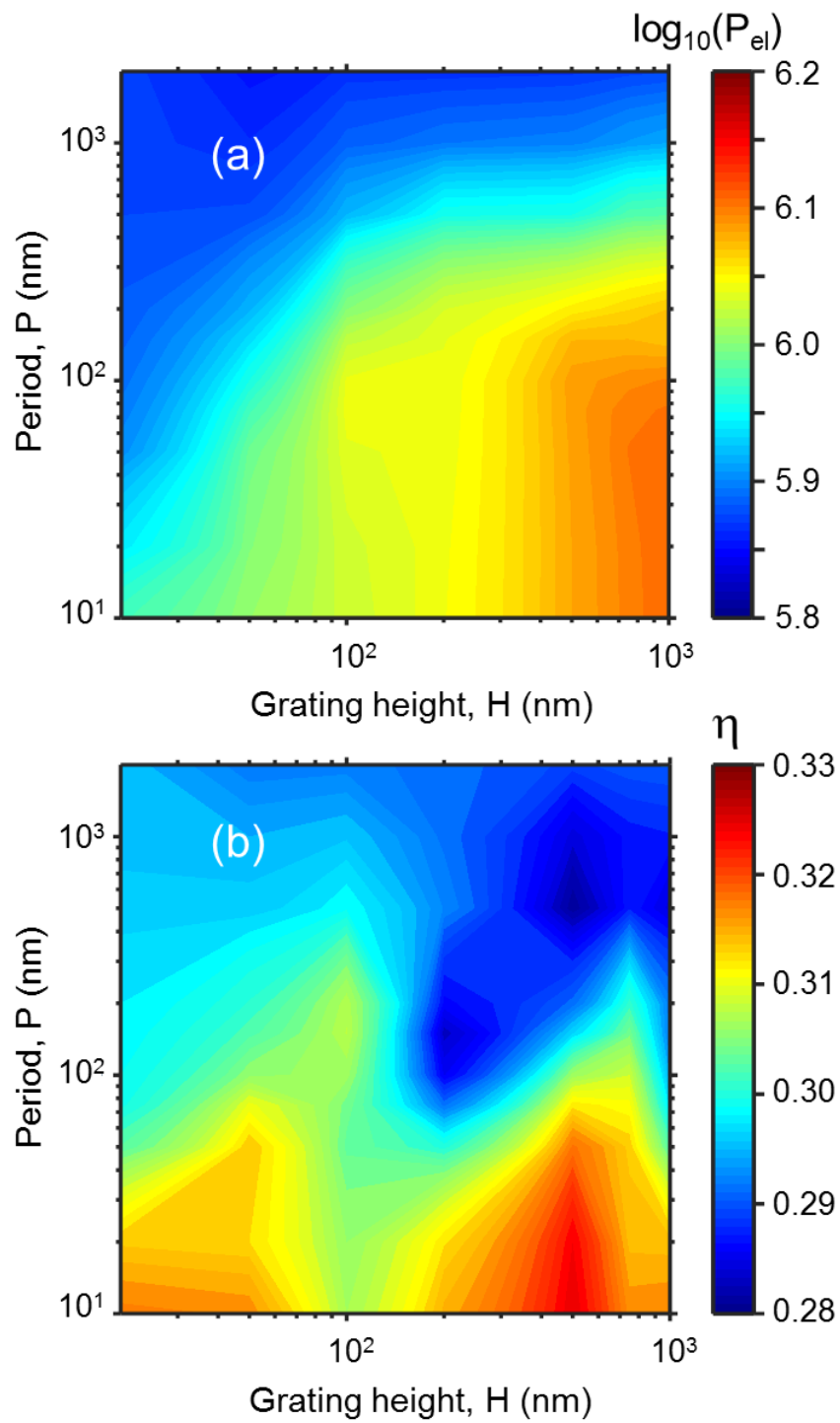
- Fig. 1 Schematic of the NFTPV device showing the coordinate axes, vacuum gap spacing d , and the geometric grating parameters: period P , height H , and ridge width w . The temperatures of the emitter at T_1 , and receiver at T_2 are specified.
- Fig. 2 Contour plots showing electric power output and conversion efficiency versus grating period and height: (a) Electrical power output in log scale, where P_{el} is in $[W/m^2]$, for the filling ratio corresponding to the highest power output. (b) Conversion efficiency for the filling ratio with the highest efficiency. Note that all calculations are at a gap spacing $d = 20$ nm.
- Fig. 3 (a) Power output and (b) conversion efficiency for the selected grating and planar tungsten emitters. The default parameters of the selected grating are $P = 50$ nm, $H = 500$ nm, and $f = 0.8$.
- Fig. 4 Parametric study for the performance when a single parameter f , P , or H is varied while the others are fixed to the default values of the selected grating. Effects of (a) filling ratio; (b) grating period; (c) grating height.
- Fig. 5 Contour plots for energy transmission coefficient at $k_y = 0$ for two cases: (a) plain tungsten without grating; (b) tungsten grating with default parameters. The white dashed line represents the light line.
- Fig. 6 Integrated energy transmission coefficient over k_x : (a) plain tungsten without grating; (b) tungsten grating with default parameters.
- Fig. 7 Spectral energy transmission coefficient for the grating and planar geometries. The band gap corresponding to 8.4×10^{14} rad/s is shown with a dotted vertical line.

Table 1. Selected sets of grating parameters from the parametric sweep that have high performance in terms of both the power output and conversion efficiency at $d = 20$ nm. Note that the power output and conversion efficiency for planar tungsten emitter is 764 kW/m^2 and 29.9%, respectively.

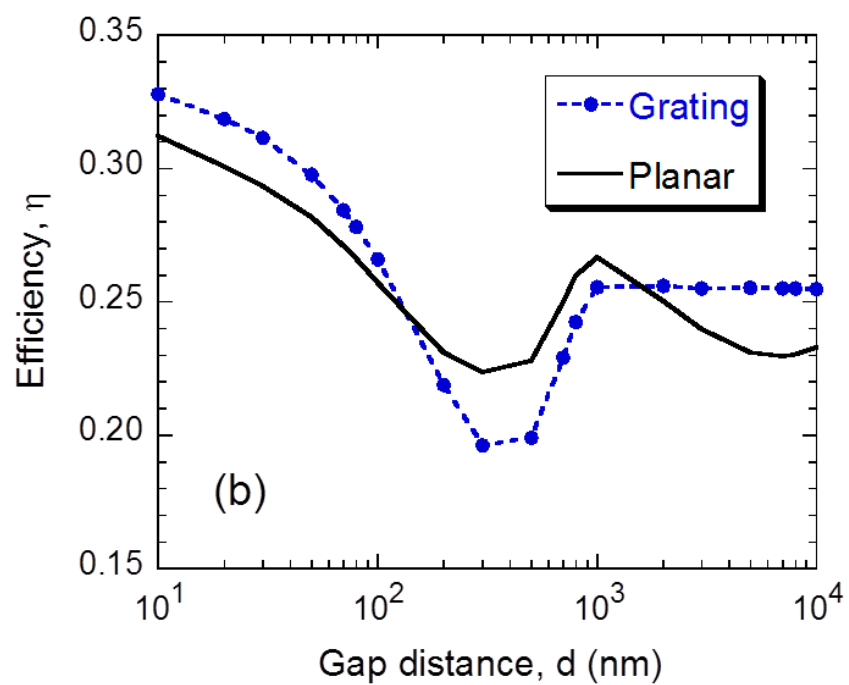
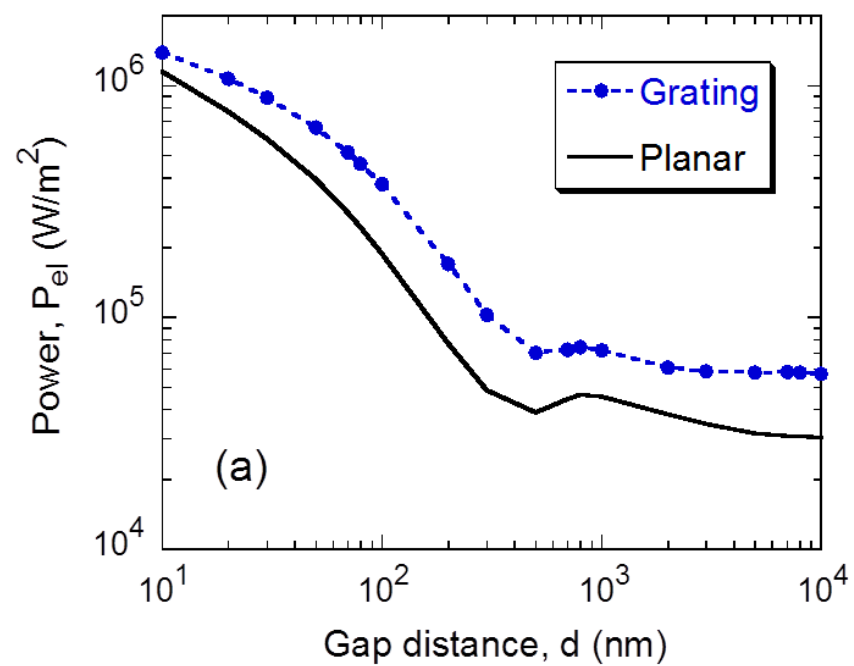
Period P (nm)	Height H (nm)	Filling ratio f	Power P_{el} (kW/m ²)	Efficiency η (%)
50	500	0.8	1078	32.0
75	750	0.5	846	31.3
150	750	0.7	1014	30.2
200	100	0.9	1009	30.9



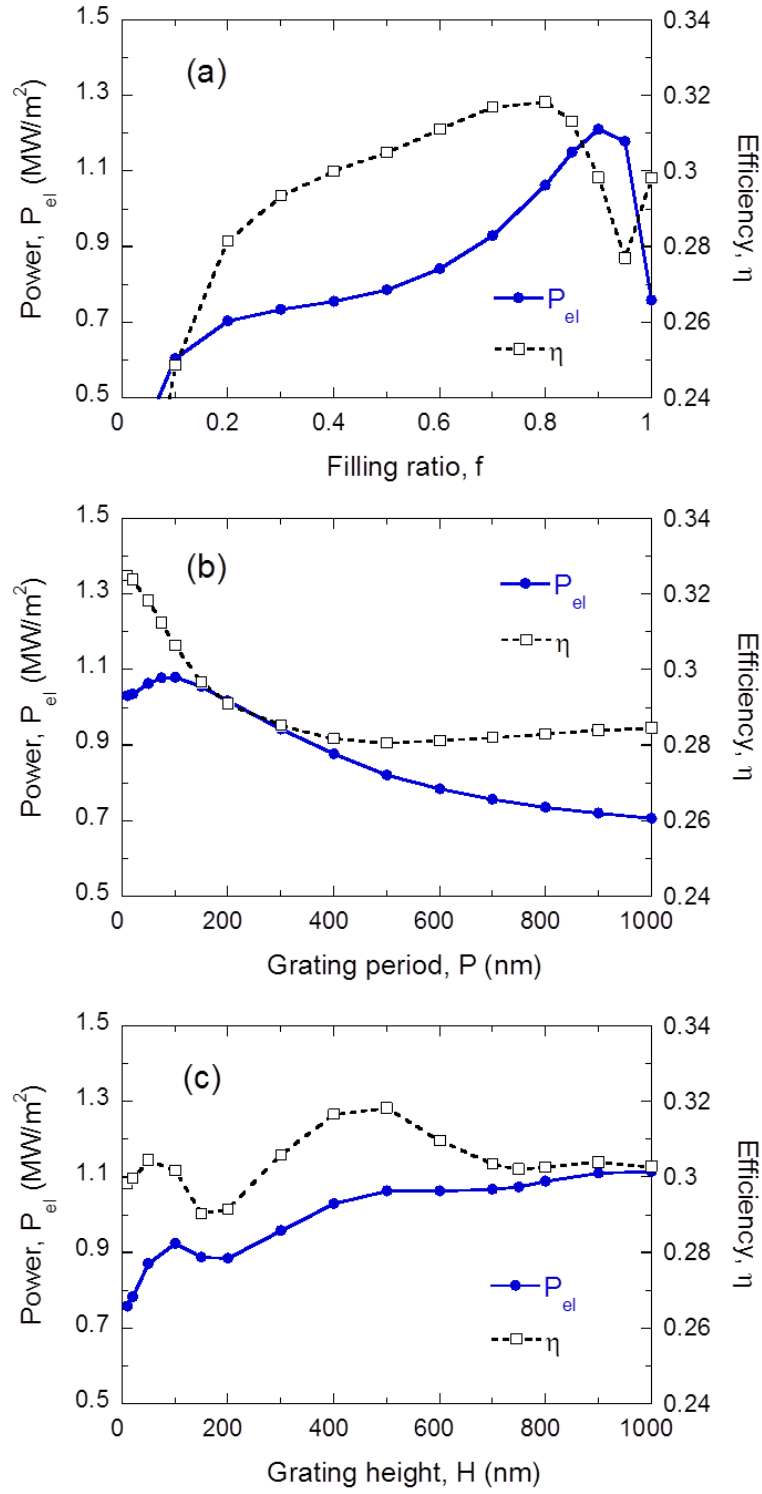
Watjen et al., Figure 1



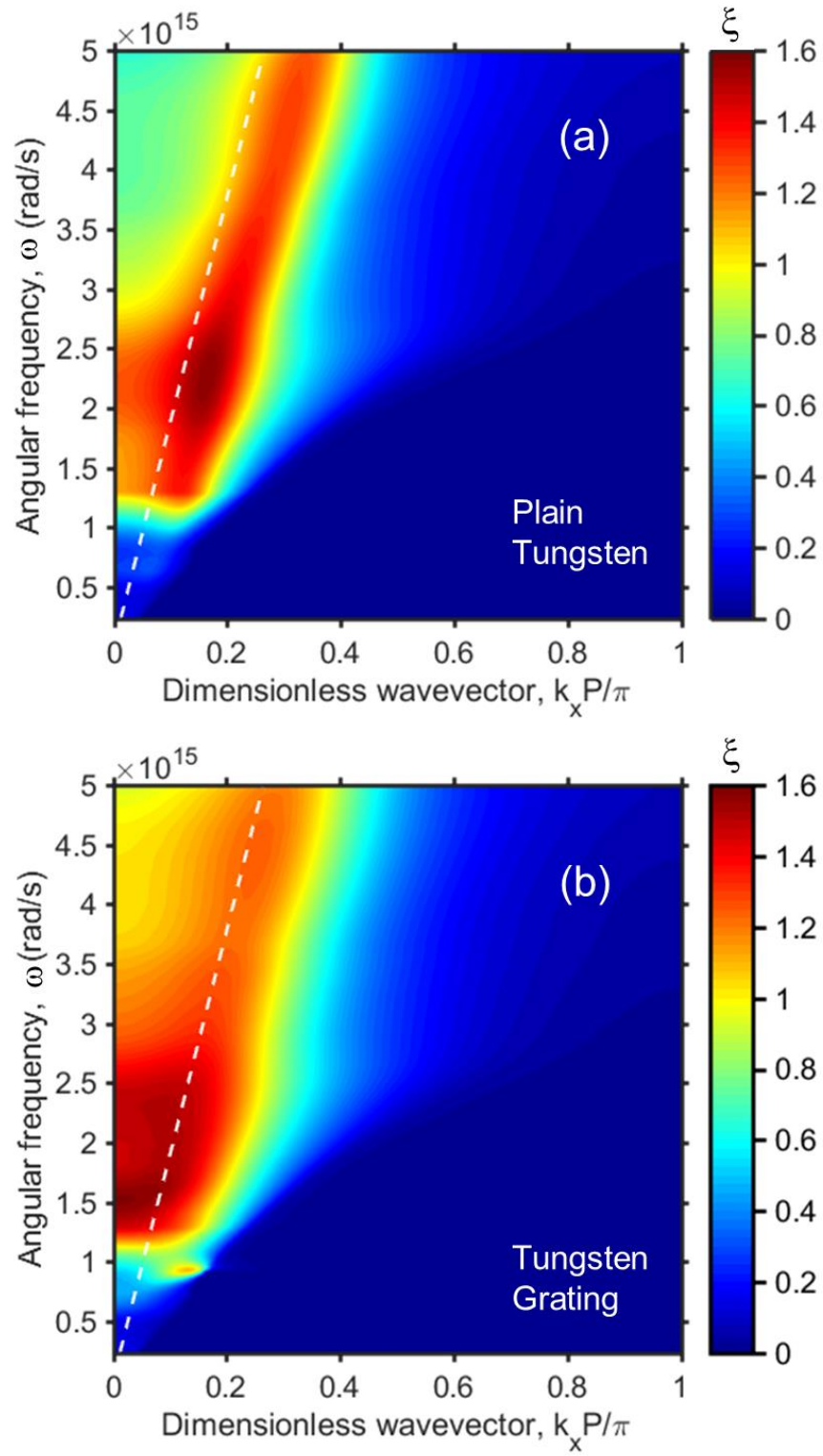
Watjen et al., Figure 2



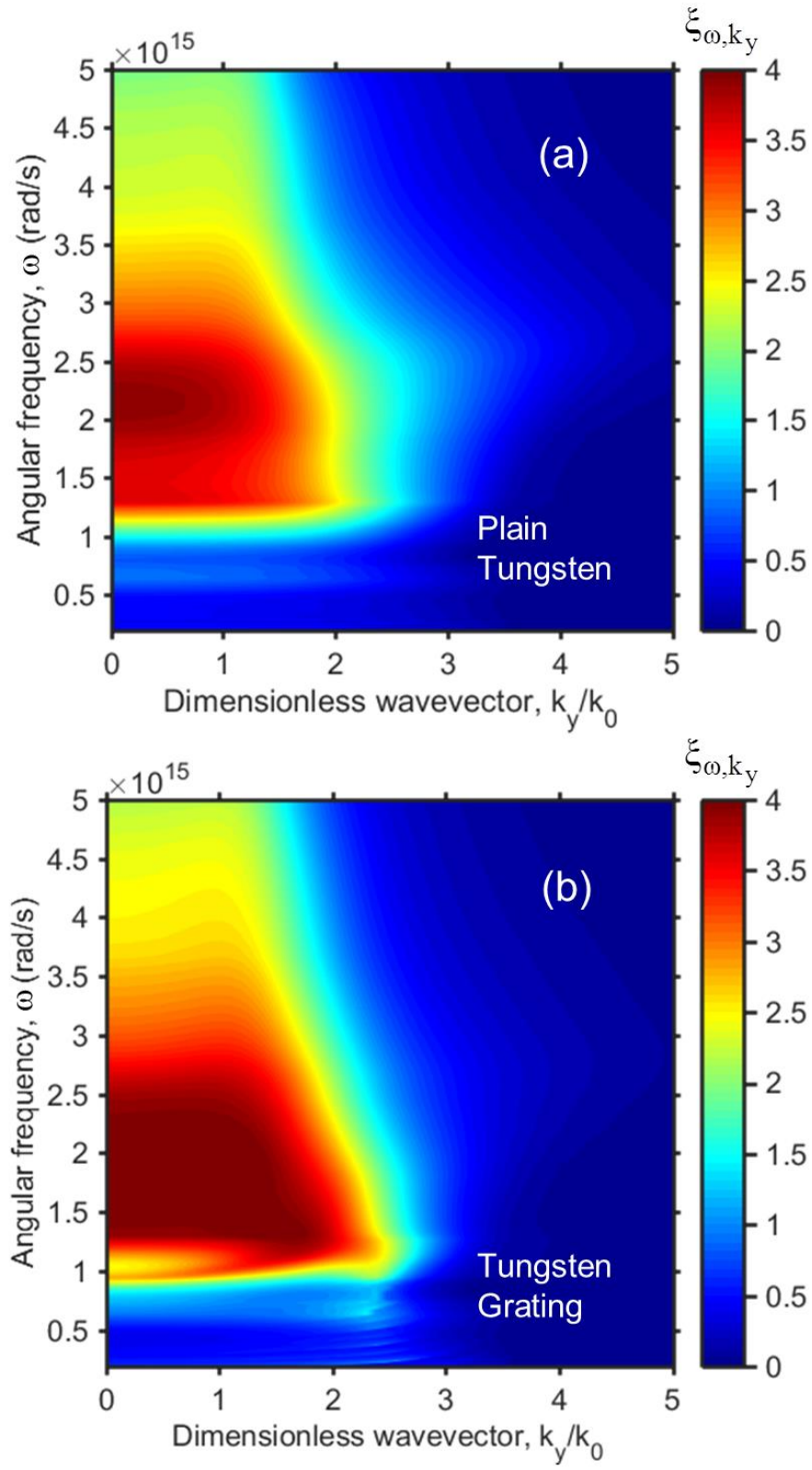
Watjen et al., Figure 3



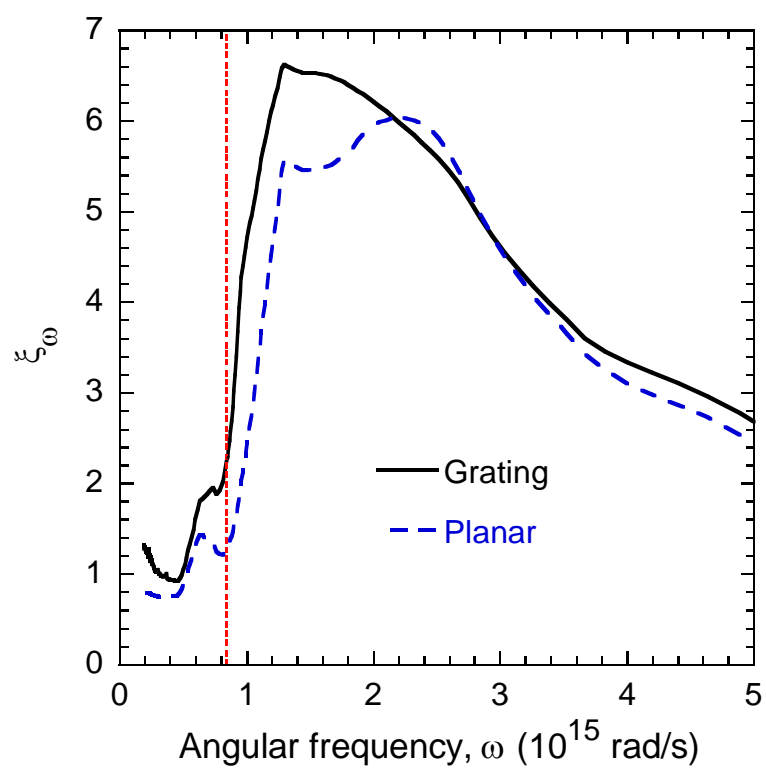
Watjen et al., Figure 4



Watjen et al., Figure 5



Watjen et al., Figure 6



Watjen et al., Figure 7